Simultaneous pseudocapacitive oxidation and oxygen evolution reaction: reciprocity or incompatibility?

Xinpeng Huang[a], Yingnan Yan[a], Xuehua Yan[a,b,*], Qianzuo Liu[a], Feng Zhang[a], Jili Wu[a], Jianmei Pan[a], Zohreh Shahnavaz[b], Jamile Mohammadi Moradian[b]

[a]*School of Materials Science and Engineering, Jiangsu University, Zhenjiang 212013, Jiangsu, China*

[b]*Institute for Advanced Materials, Jiangsu University, Zhenjiang 212013, Jiangsu, China*

*Corresponding author: Xuehua Yan: xhyan@ujs.edu.cn

EXPERIMENT SECTION

1. Reagents and raw materials

All reagents used in this work were analytical reagents. The reagents used include $NiCl_2·6H_2O$, $CoCl_2·6H_2O$, $AlCl_3·6H_2O$, $FeCl_3·6H_2O$, $CuCl_2·2H_2O$, CH_4N_2O, KOH, H_2SO_4, HNO_3 that were purchased from Sinopharm Chemical Reagent Co., Ltd, China. Carbon cloth (CC) was purchased from CeTech Co., Ltd. And the deionized water was obtained by SCSJ-II-20L in our lab. All reagents were directly used as received.

2. Samples preparation

The substrate used for the self-grown samples was 1 cm×1 cm carbon cloth, which was activated before use as follows: the carbon cloth was immersed in 10 wt.% nitric acid and 10 wt.% sulfuric acid in a volume ratio of 3:1 for 6 h, followed by sonication in water and anhydrous ethanol alternately for 10 min each to wash off the nitric acid and sulfuric acid, and vacuum dried for use. The effectively exposed area of each electrode is 1 cm^2 (2×1 cm×0.5 cm) in the electrochemical test, due to half of the raw area being sealed by the electrode holder.

The samples in this work are all self-grown and respectively named M^2 (NiCo), M^3 (NiCoAl), M^4 (NiCoAlFe), and M^5 (NiCoAlFeCu) according to the kinds of metal elements contained in samples. The preparation process was as follows: the corresponding hydrates and the corresponding amount of urea were weighed and added into 60 mL of deionized water. Activated carbon cloth was immersed in the solution with magnetic stirring for 6 h. Subsequently, the solution and carbon cloth were transferred to a stainless steel autoclave with a Teflon liner for a hydrothermal reaction at 100 °C for 12 h. After the reaction was finished, the reaction vessel was cooled to room temperature in air and washed with deionized water and anhydrous ethanol 4 times alternatively. Finally, the samples were dried in a vacuum at 60 ℃ for 24 h. The amounts of each hydrate (0.002 mol) were as follows, 0.4752 g for $NiCl_2·6H_2O$, 0.4756 g for $CoCl_2·6H_2O$, 0.4826 g for $AlCl_3·6H_2O$, 0.5404 g for $FeCl_3·6H_2O$, and 0.3409 g for $CuCl_2·2H_2O$. The weight of various hydrates was the same for different samples with only different types of hydrates added. To match the metal dosages, the urea dosages for different samples were as follows, 0.6 g for M^2, 0.9 g for M^3, 1.2 g for M^4, and 1.5 g for M^5. Details of the characterizations and tests were listed in the supplementary information too.

3. Characterization

The XRD data were measured using Rigaku Ultimate IV Powder X-ray from Japan, whose X-ray source was Cu Ka, with a wavelength of 1.5418 Å, a voltage of 40 KV, and a current of 40 mA. Transmission electron microscope (TEM) images were obtained through Hitachi HT-7800, and selected area electron diffraction (SEAD) and high-resolution TEM (HR-TEM) images were taken through FEI TF-G20. Scanning electron microscopy (SEM) observations were performed with the aid of Hitachi Regulus 8100 and FEI QUANTA 250 FEG. Fourier Transform infrared spectroscopy **(**FT-IR) was obtained by Thermo Scientific Nicolet iS20, and the test was performed by acquiring the background and then the IR spectrum of the sample, with a resolution is 4 cm^{-1}, 32 scans, and a test wavenumber range of 400-4000 cm^{-1}. The XPS data were obtained by Thermo Scientific K-Alpha with an excitation source of Al Kα rays (hv=1486.6 eV), and the sample was fed into the analysis chamber when the pressure in the chamber was less than 2.0×10^{-7} mbar. The testing spot size is 400 μm, with an operating voltage of 12 kV, and a filament current of 6 mA. The full-spectrum scan fluence energy was 150 eV in steps of 1 eV; the narrow-spectrum scan fluence energy was 50 eV in steps of 0.1 eV, and the narrow-spectrum signal was accumulated for at least 5 cycles. The data were rectified based on C1s = 284.80 eV binding energy as standard. The UV-vis DRS test was conducted using Shimadzu UV-3600i Plus, with a starting wavelength of 800 nm and an ending wavelength of 200 nm, a data interval of 1.0 nm, a scanning speed of medium speed, and a slit width of 20. The Tauc plot is obtained by modifying Tauc's method according to Equation S1. The Mott-Schottky plots were obtained through the impedance potential (IMPE) test with the aid of CHI 760E in a three-electrode system, including prepared samples loaded on FTO conductive glass (20 mm×10 mm×1.1 mm, ρ is about 15 Ω) as work electrode, Pt plate as the counter electrode, Ag/AgCl as the reference electrode, and 0.5 M Na_2SO_4 as electrolyte. The IMPE testing parameters are as follows, the amplitude is 0.01 V, the frequency is 1000 Hz, and the testing voltage range is set with a stable open circuit voltage as the center and a width of 1 V. The data processing is based on Equation S2.

4. Electrochemical test

All electrochemical performances were tested via the CHI 760E. All three electrode systems run in the PTFE electrolytic cell. Due to all prepared samples being self-grown samples, the performances of naked carbon cloth (CC) which experienced activating treatment was also tested, to eliminate the influence of the substrate.

4.1 OER Electrocatalysis:

The electrocatalytic oxygen evolution reaction (OER) performances of samples were tested in a three-electrode system, containing a working electrode with a total exposed area of 1 cm^2, a graphite rod (Φ6 mm×60 mm, immersed length 20 mm) as the counter electrode, and a Hg/HgO as a counter electrode with an electrolyte of 1 M KOH. Oxygen was continuously introduced into the electrolyte for 30 min before the test to fix the reversible potential of oxygen. Before the OER performance tests, we apply CV method cycled (20 times) the test system at a small scan rate of 5 mV/s to activate it. The voltage range for this CV cycle (activated process) was 0-0.7V (vs Hg/HgO reference electrode potential), which totally covers the pseudocapacitive reaction rang. All tests were performed without automatically IR compensation. Linear sweep

voltammetry (LSV) tests were performed at a scan rate of 5 mV s^{-1}. The calculation of potential is based on Eqs. S3-S5. A linear fit was performed to obtain the Tafel slope according to Eq. S6 and LSV data. The cyclic voltammetry (CV) tests were carried out at a scan rate of 10 mV, 20 mV, 40 mV, 60 mV, 80 mV, and 100 mV, taking the potential of 0.1 V (vs Hg/HgO) in the non-Faraday reaction interval as the center and taking the potential window of 0.1 V. The average currents of the CV curves obtained at 0.1 V for each scan rate were taken and linearly fitted according to Eq. S7-S8 to get the corresponding C_{dl} values for each sample. Before EIS tests, the stable open circuit potential is tested through the open circuit potential-time (OCPT) function, which is used as the bias voltage for EIS testing. OER catalysis stability of samples was tested by the multi-current steps (ISTEP) function, but each test was set for only one step of current, allowing the sample to run at a constant current for an extended period to observe the overpotential changes. Data of 10 mA and 100 mA constant current tests are saved by least-squares smoothing skipped 21 and 49 points, respectively. For an in-depth analysis of the material evolutions before and after the long-time constant current test, CV with a potential window of 0-0.7 V (vs Hg/HgO) and EIS were performed after every constant current test, and the EIS curves after each constant current test were not fitted for a realistic and intuitive comparison. After a total duration of 32 h in the 10 mA constant current test, two 500 cycles of CV scans with a scanning rate of 100 mV were performed on the tested sample in the range of 0-0.7V (vs Hg/HgO). The corresponding EIS was also tested after both 500 cycles of CV tests.

4.2 Pseudocapacitive energy storage:

The pseudocapacitive energy storage tests were implemented in a three-electrode system with a Pt plate (10 mm×15 mm×0.1 mm) as the counter electrode, Hg/HgO as the reference electrode, and 1 M KOH as the electrolyte. The galvanostatic charge/discharge (GCD) curve obtained by chronopotentiometry test, sets the corresponding current according to the actual load and current density value of the sample. Specific capacitances were calculated by Eqs. S9-S10. According to Eq. S11, all coulombic efficiencies are calculated from the charge/discharge energy values counted in the CHI 760 exported data. The capacitance retention of cyclic charging and discharging is calculated by taking the discharge capacity of an integer multiple of 500 cycles. The fact total charge and discharge cycles are 10000 cycles. The EIS test bias voltage uses a stable open circuit potential.

5. Equation used:

$$(\alpha h\nu)^n = K(h\nu - E_g) \quad \textbf{(S1)}$$

where α is absorption value; h is Planck constant; v is frequency; E_g is the band gap; and n takes 2. The E_g was obtained from the x-intercept by corresponding linear fitting [1, 2].

$$\frac{1}{C^2} = \frac{2}{\varepsilon\varepsilon_0 e N_d}\left(V - V_{FB} - \frac{K_B T}{e}\right) \quad \textbf{(S2)}$$

where C is interfacial capacitance (F cm^{-2}); N_d is the carrier density (cm^{-3}); V is the applied potential; e is an elementary charge; K is the Boltzmann's constant (1.38×10^{-23}

F m^{-1}); T is the absolute temperature (K); and V_{FB} is flat band potential. The V_{FB} could be obtained by linear fitting based on Equation S2 [3, 4].

The potentials obtained by Hg/HgO as reference electrode were converted to a reversible hydrogen electrode (RHE) by the following Equation S3 [5]:

$$\mathbf{E_{RHE} = E_{Hg/HgO} + 0.0592 \times PH + 0.098} \quad \textbf{(S3)}$$

The potentials obtained by Ag/AgCl as reference electrode were converted to a reversible hydrogen electrode (RHE) by the following Equation S4 [6]:

$$\mathbf{E_{RHE} = E_{Ag/AgCl} + 0.0592 \times PH + 0.197} \quad \textbf{(S4)}$$

The overpotential (η) of OER is calculated by the following Equation S5 [5]:

$$\boldsymbol{\eta = E_{RHE} - 1.23} \quad \textbf{(S5)}$$

The Tafel value is calculated by linear fitting slope value according to the following Equation S6:

$$\boldsymbol{\eta = a + b\log_{10}|i|} \quad \textbf{(S6)}$$

where the η is overpotential and i is current density [6].

The electrochemical active area (ECSA) is proportional to double-layer capacitance (C_{dl}) as seen in the following Equation S7:

$$\mathbf{ECSA = C_{dl}/C_s} \quad \textbf{(S7)}$$

where the Cs is the specific capacitance of the corresponding surface smooth sample under the same conditions [7].

The double layer capacitance (C_{dl}) is measured from the CV curves at different scan rates based on the following Equation S8. The range of applied potentials taking no significant Faraday process occurs is determined from the static CV curve, which is operated through a potential window of 0.1 V at the center of the open circuit potential (OCP).

$$\boldsymbol{i_c = v\,C_{dl}} \quad \textbf{(S8)}$$

where the i_c is the current (A) of the double-layer capacitor and v is the applied potential (V) [7].

The specific capacitances based on GCD curves are calculated according to the following Equation S9:

$$\mathbf{C_m = 2I\int vdt/m\Delta V} \quad \textbf{(S9)}$$

where C_m is specific capacitance (F g^{-1}); I is current (A); V is applied potential (V); m is loading mass of active material; ΔV is working potential window [8].

The specific capacitances based on CV curves are calculated according to the following Equation S10:

$$\mathbf{C} = \frac{\mathbf{A}}{\mathbf{2mk(\Delta V)}} \quad \textbf{(S10)}$$

where C is specific capacitance (F g^{-1}); A is the area of CV curve covered; k is scan rate; m is loading mass of active material; ΔV is working potential window [9].

The coulombic efficiency is calculated according to Equation S11 [8]:

$$\mathbf{EFc} = \frac{\mathbf{Energy\ density(discharge)}}{\mathbf{Energy\ density(charge)}} \quad \mathbf{(S11)}$$

where the EFc is coulombic efficiency; the energy densities (charge/discharge) were obtained from statistical results of the chronopotentiometry test by CHI760.

203
204
205
206
207

RESULTS

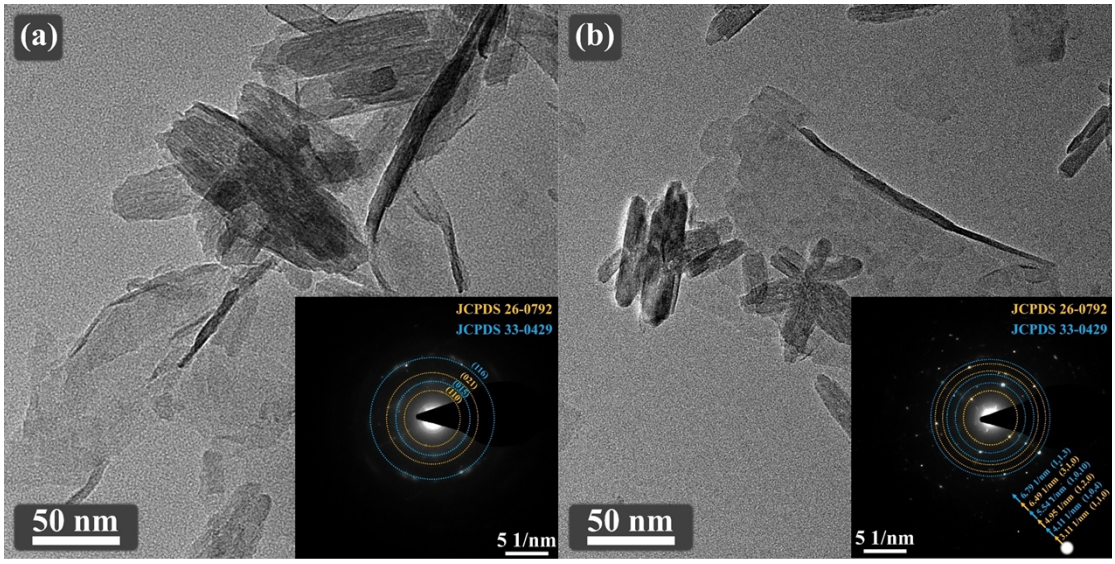

Figure S1 BF-TEM image and corresponding SAED of M^5.

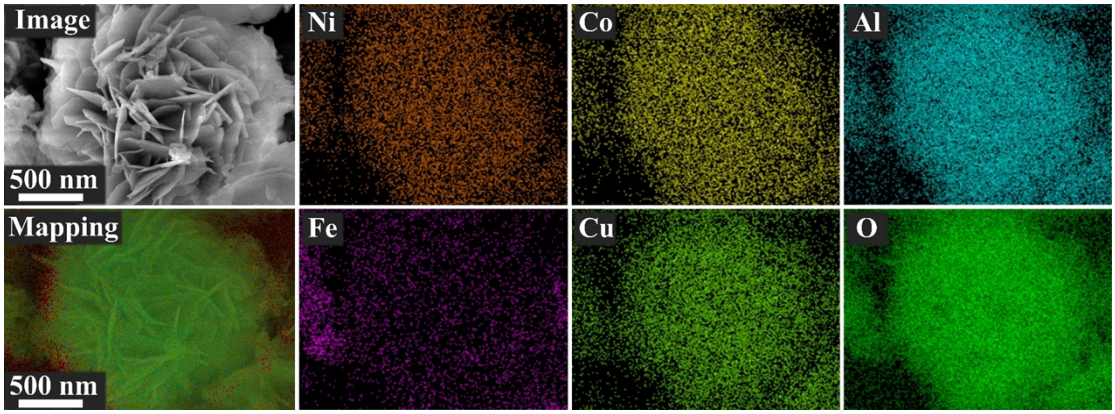

Figure S2 SEM image and corresponding area elements mappings.

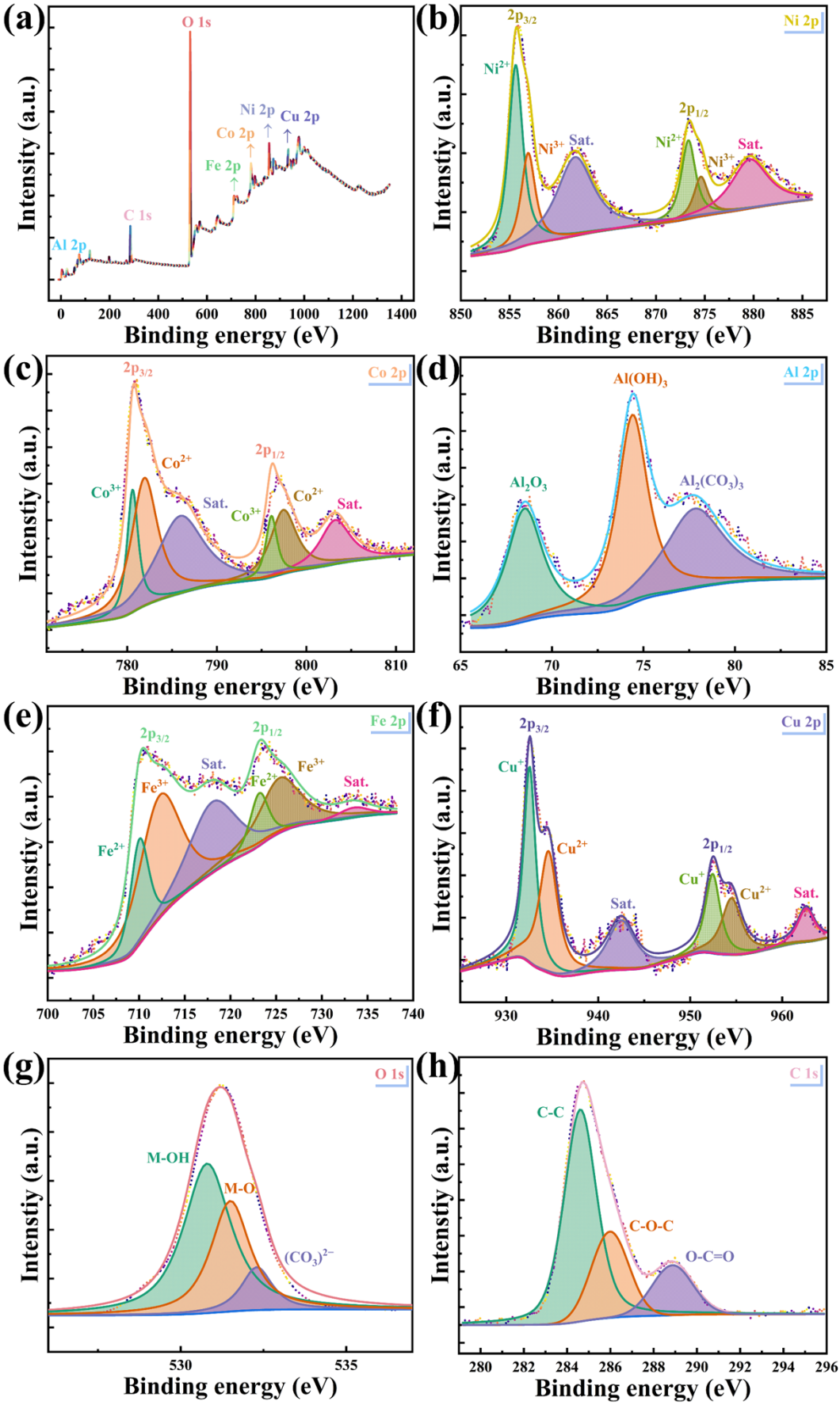

Figure S3 (a) XPS survey spectra, and (b)-(h) high-resolution XPS of different elements of M[5].

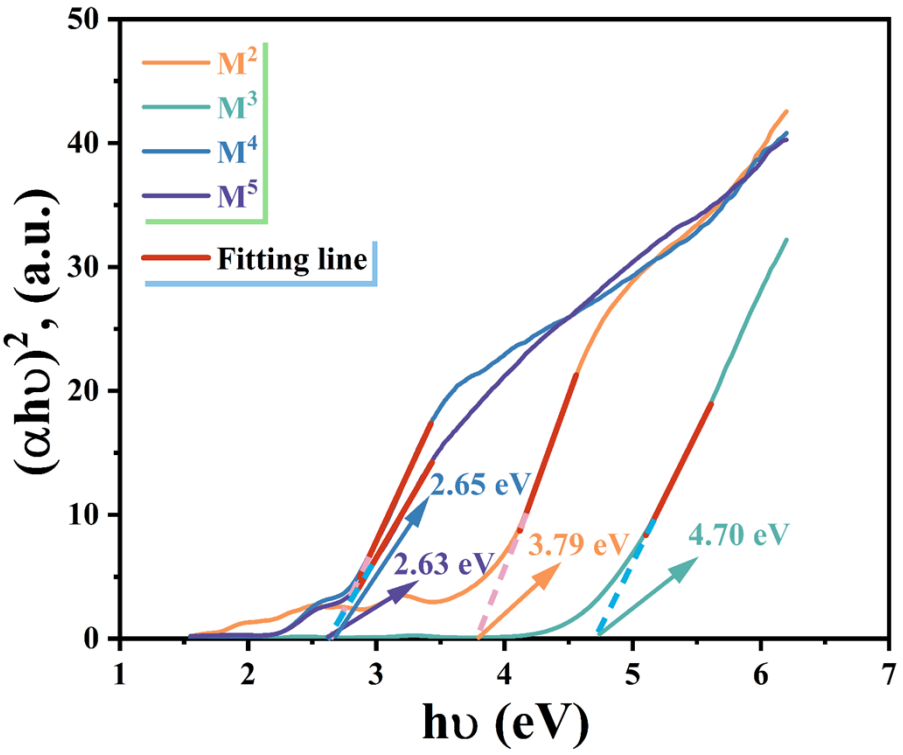

Figure S4 Tauc plot based on UV-vis results of M^2, M^3, M^4, and M^5.

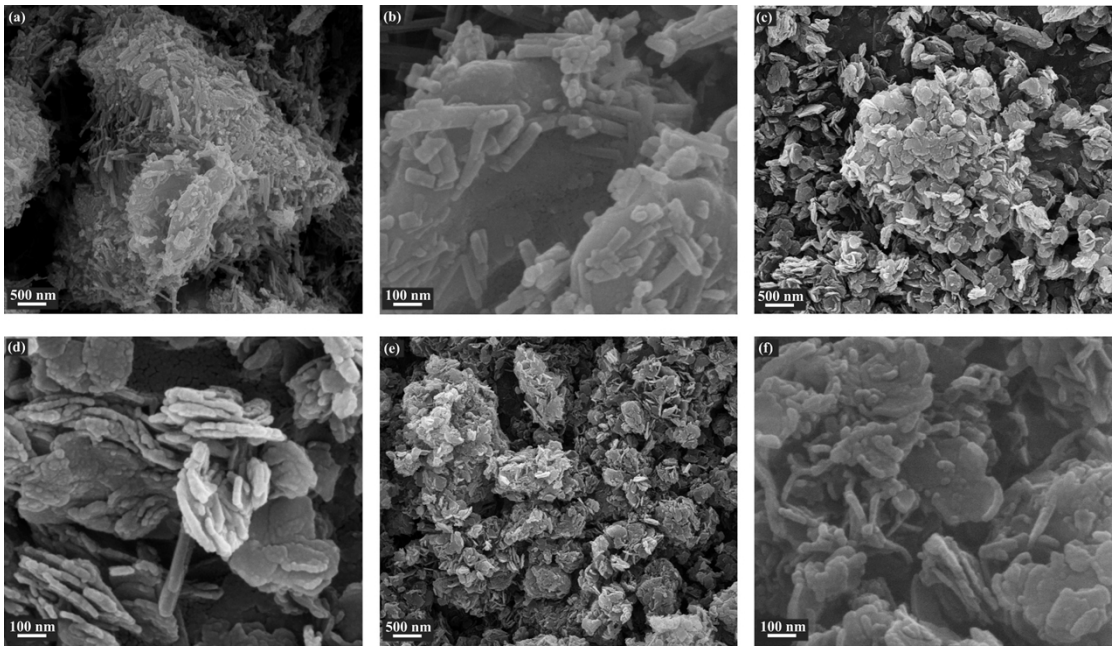

Figure S5 SEM images of (a)-(b) M^2, (c)-(d) M^3, (e)-(f) M^4.

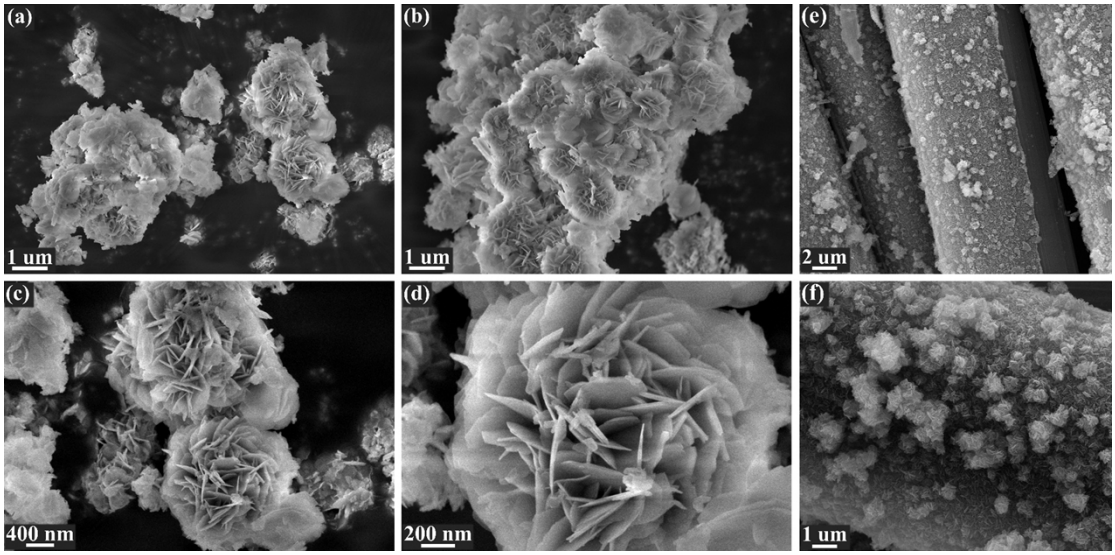

Figure S6 Different magnification SEM images: of (a)-(d) M^5 powder sample, and (e)-(f) M^5 electrode sample.

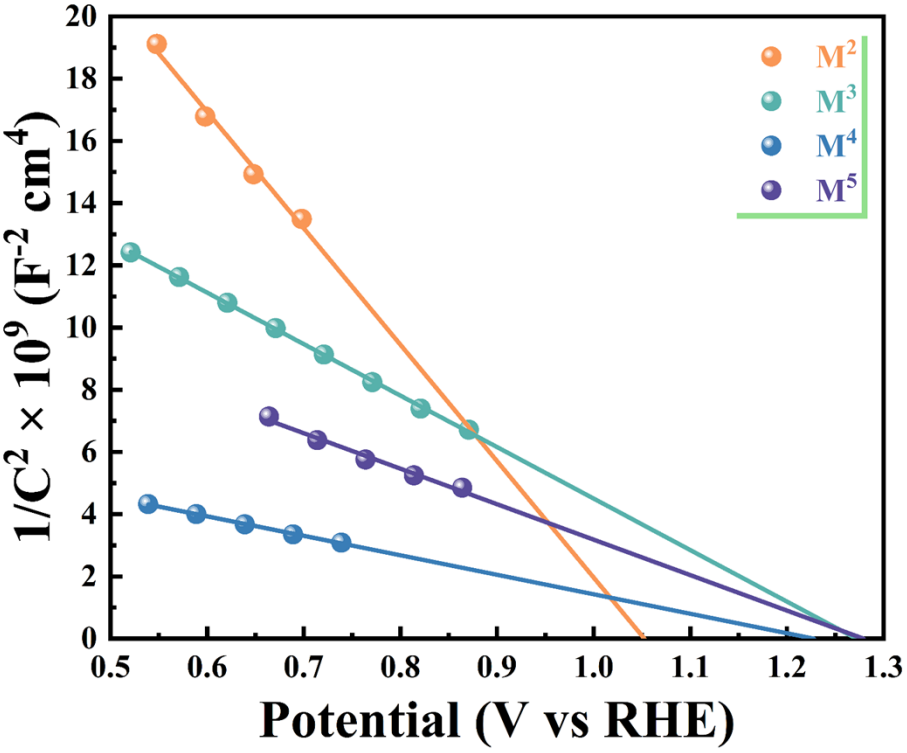

Figure S7 Mott-Schottky plot of M^2, M^3, M^4, and M^5.

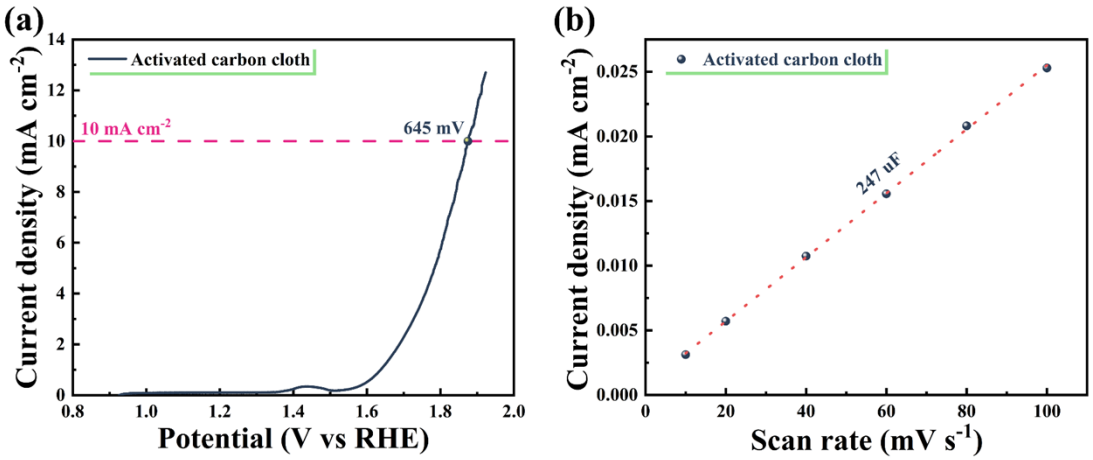

Figure S8 (a) LSV curve at 5 mV s^{-1} and (b) C_{dl} of activated carbon cloth.

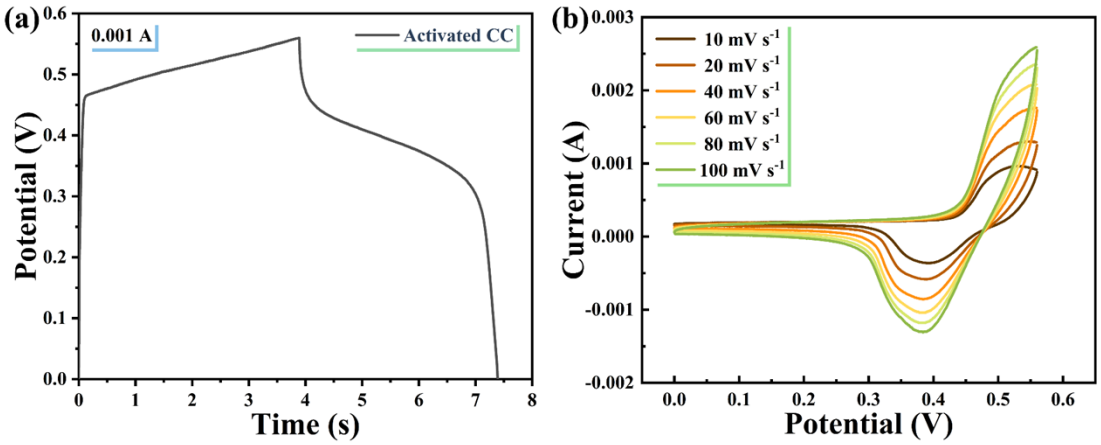

Figure S9 (a) GCD curves at 1 mA and (b) CV curves at different scan rates of activated carbon cloth.

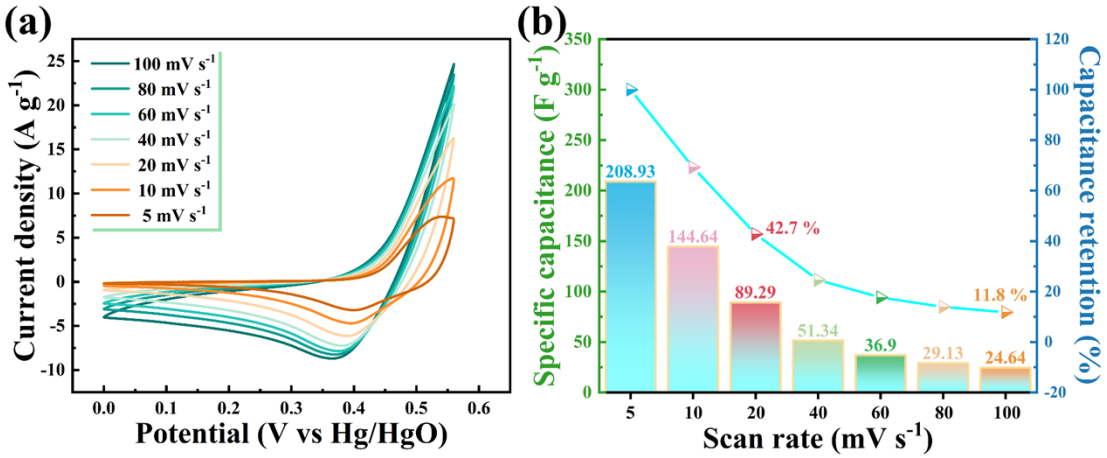

Figure S10 (a) CV curves at different scan rates and (b) specific capacitance and rate capacity of M^5 calculated by CV curves.

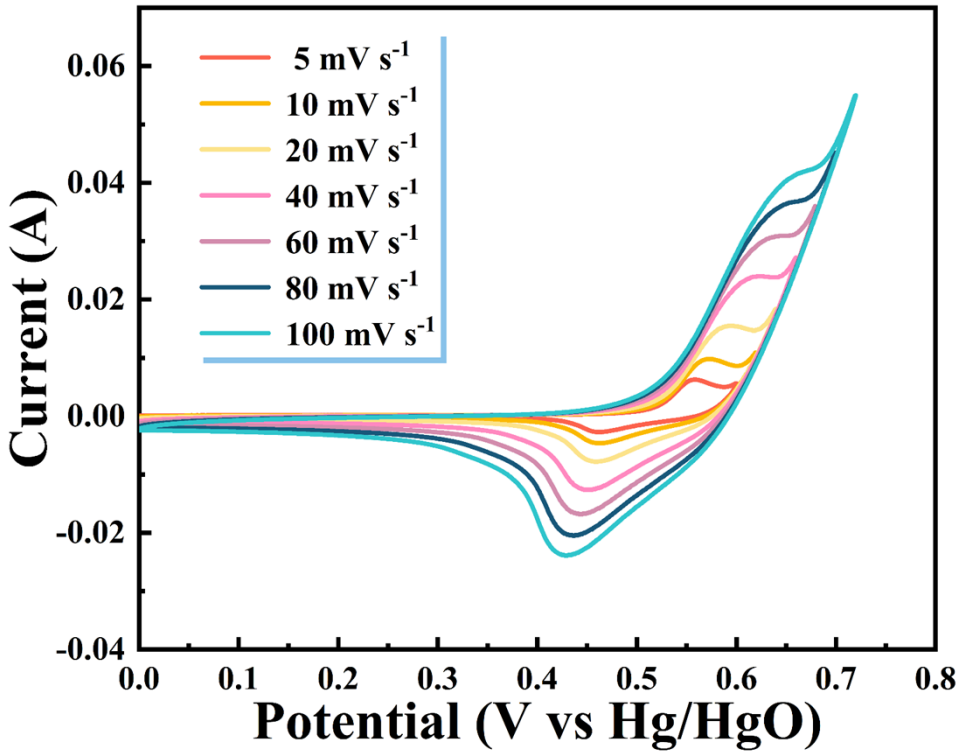

Figure S11 CV curves at different scan rates and different potential windows of M^5 (Activated by CV 20-cycles among 0-0.6 V).

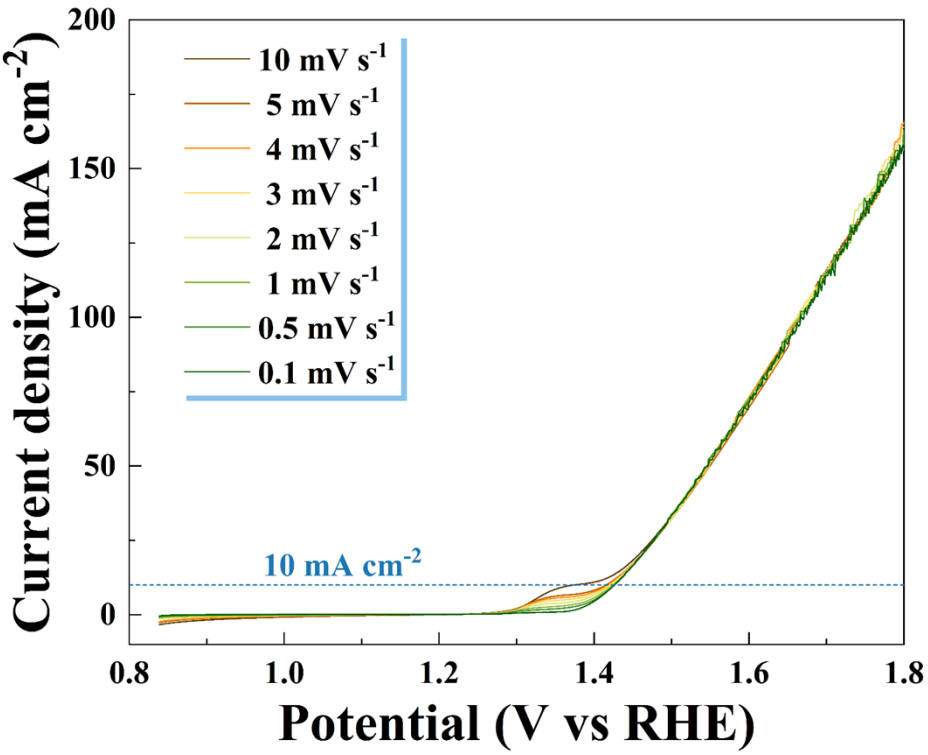

Figure S12 The LSV curves of M^5 at different scan rate.

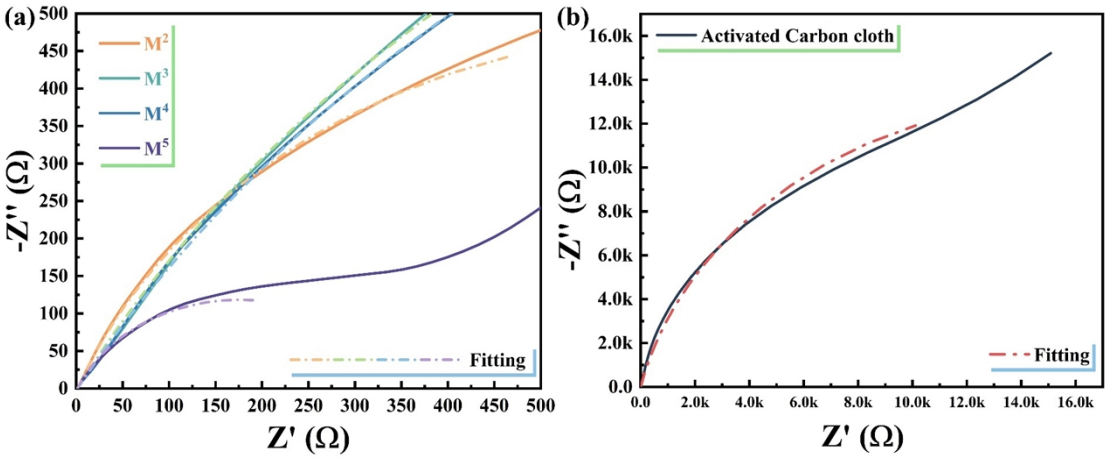

Figure S13 The EIS for OER of (a) M^2, M^3, M^4, and M^5, and (b) activated carbon cloth.

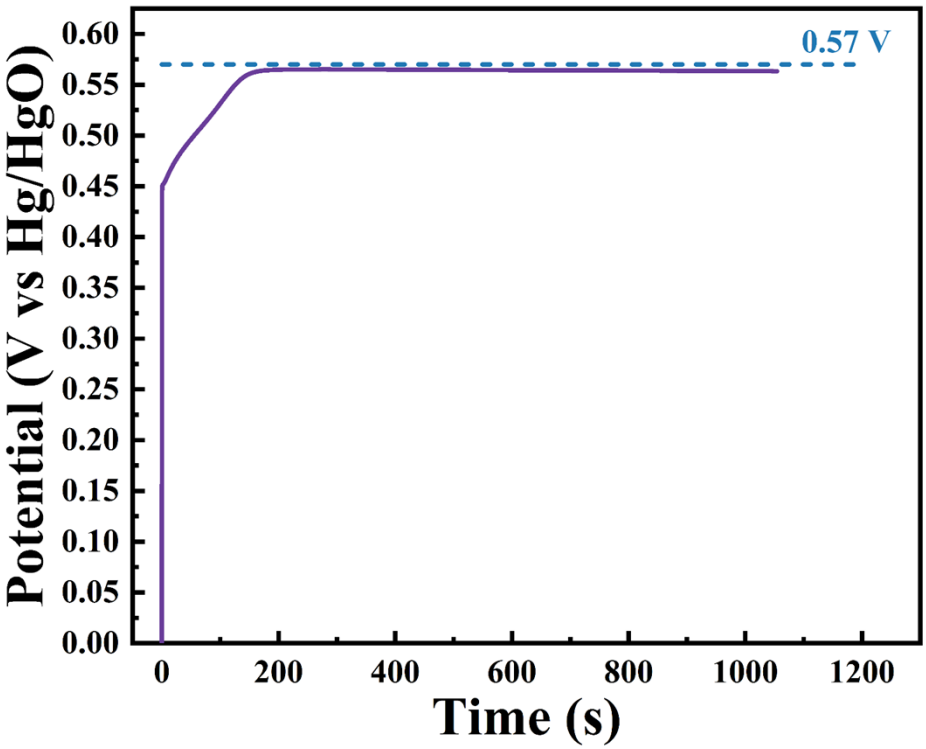

Figure S14 The charge curve of M^5 via chronopotentiometry at 1 A g^{-1}.

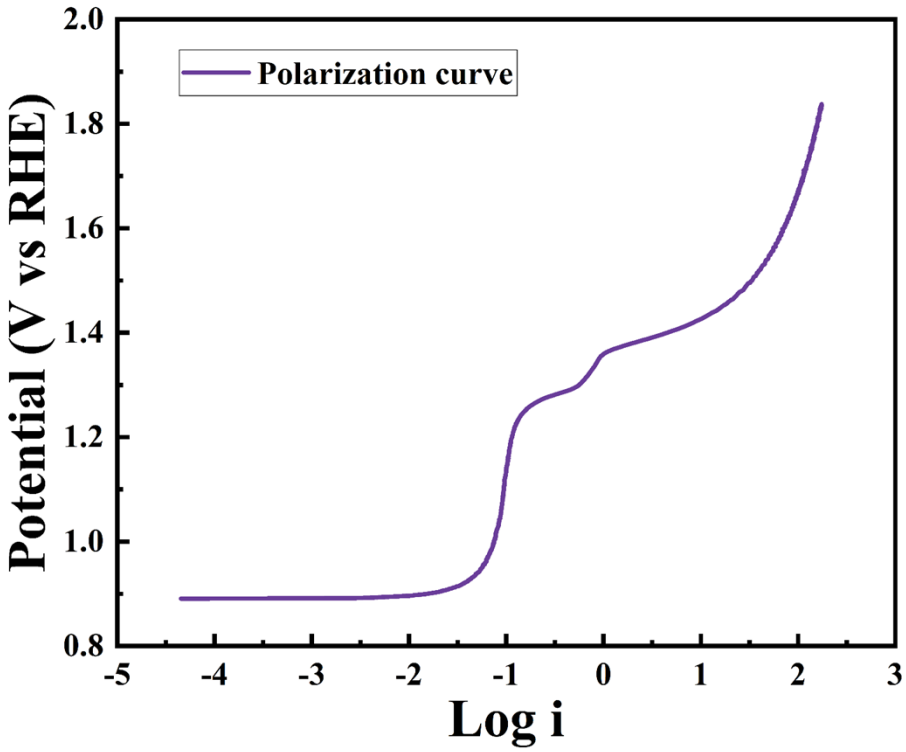

Figure S15 The polarization curves obtained by LSV at 0.1 mV s^{-1} (Quasi steady state).

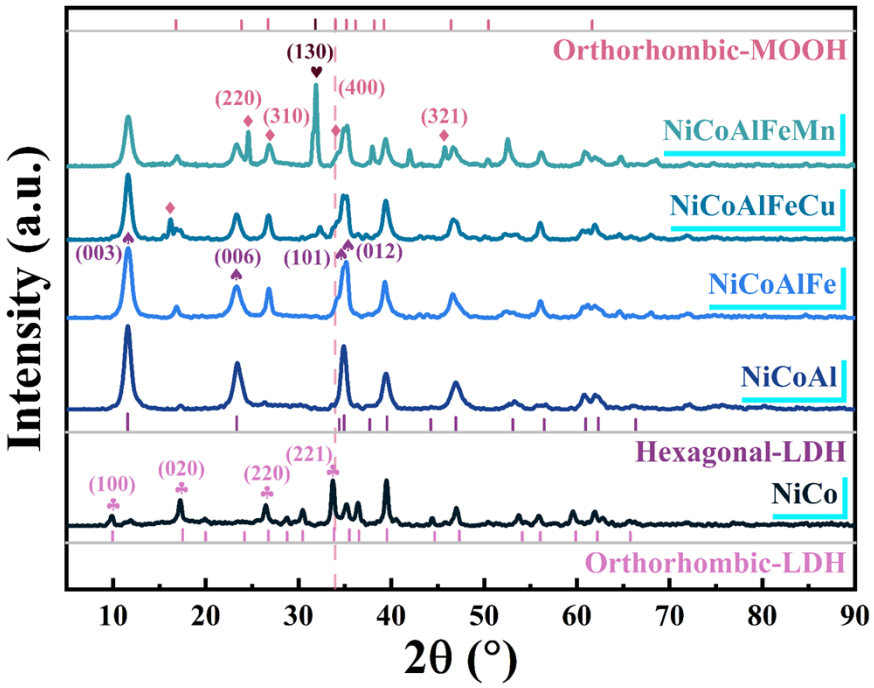

Figure S16 The XRD results of NiCoAlFeMn sample and comparison with the previously prepared samples.

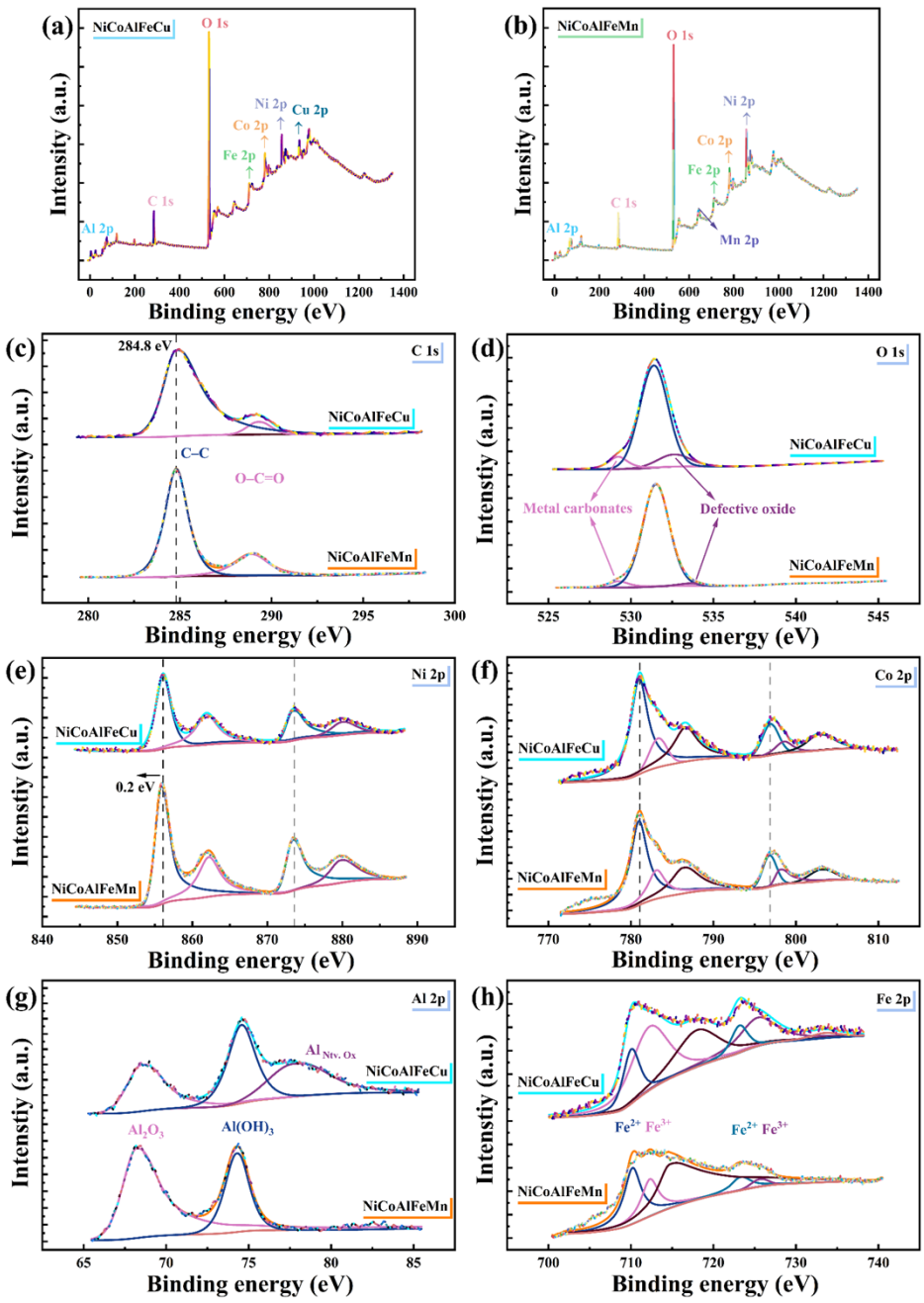

Figure S17 The XPS results of NiCoAlFeMn sample and it compares with the prepared M^5 sample.

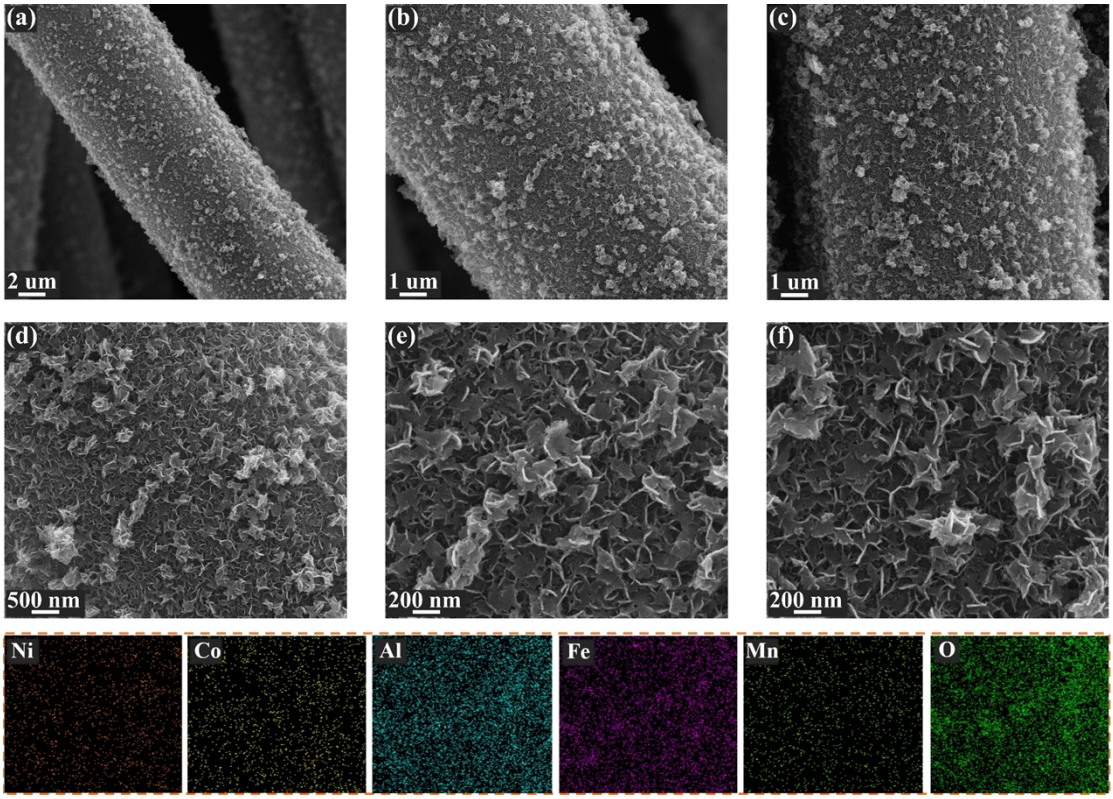

Figure S18 The SEM images and elements mapping of NiCoAlFeMn sample.

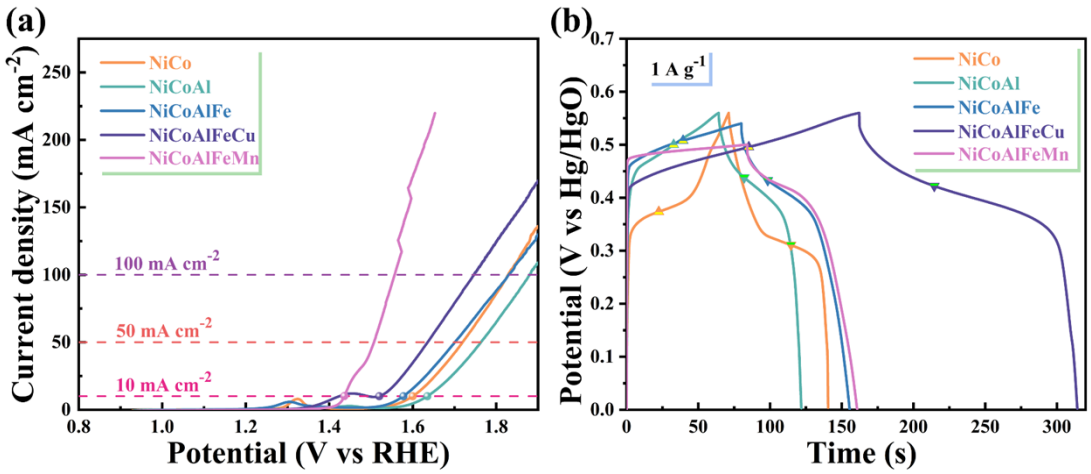

Figure S19 (a) LSV curves at 5 mV s^{-1} and (b) GCD curves at 1 A g^{-1} of NiCoAlFeMn sample and comparison with the previously prepared samples.

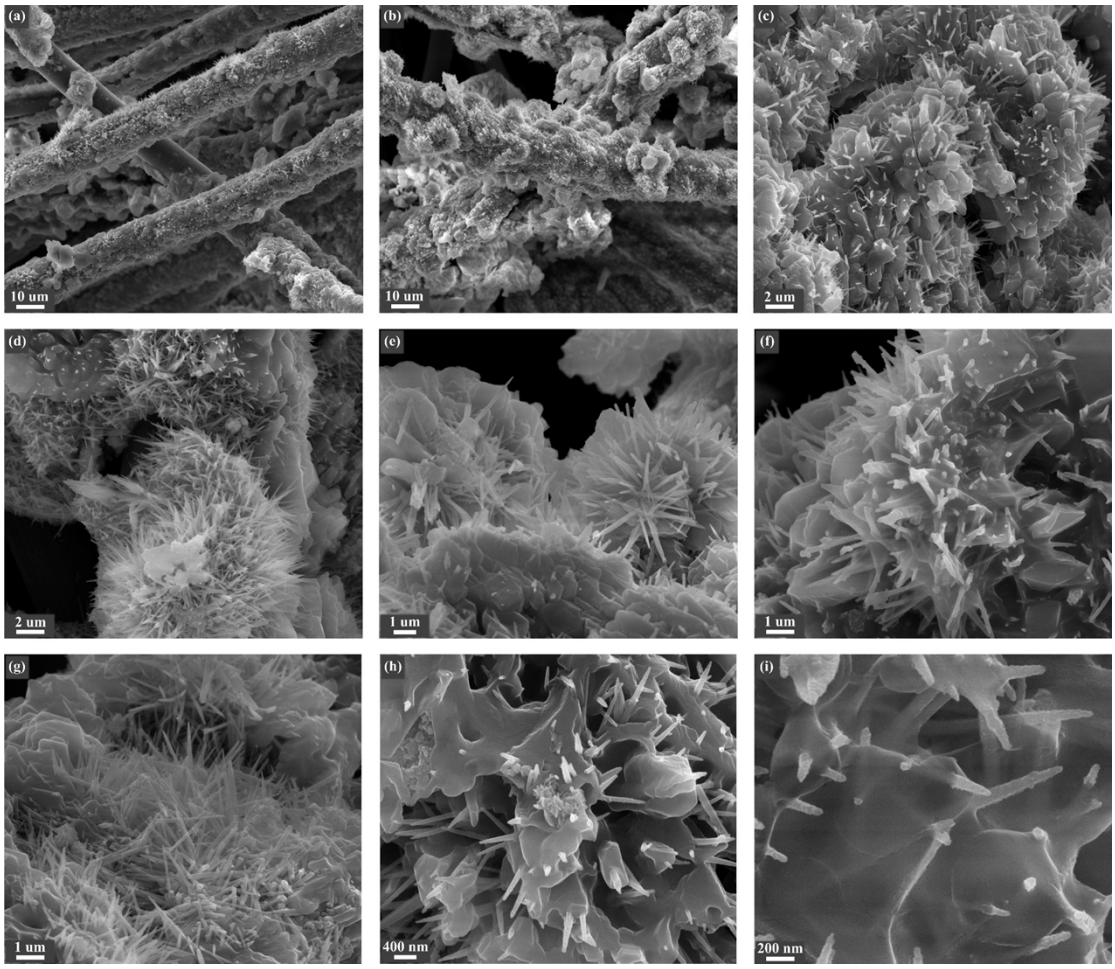

Figure S20 Different magnification SEM images of M^5 after 20 h constant current test at 100 mA cm^{-2}.

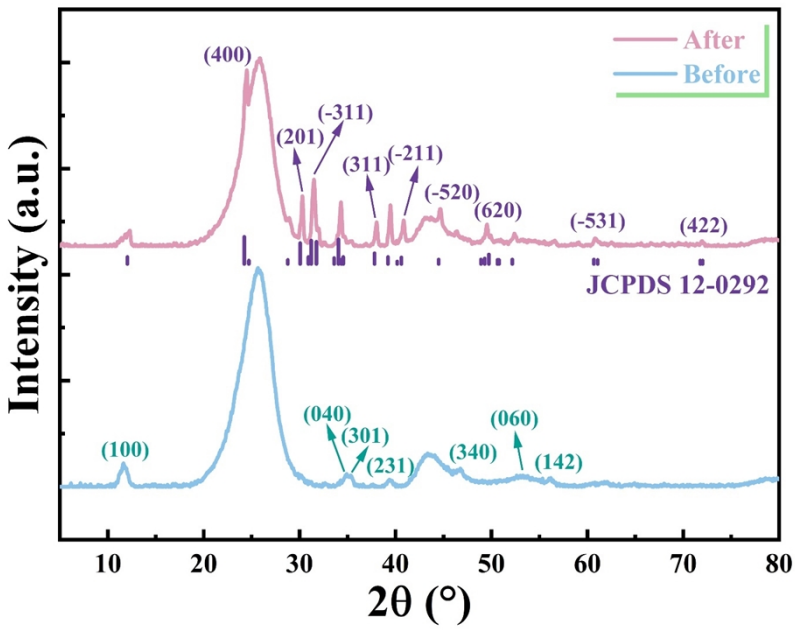

Figure S21 XRD of M^5 sample before and after 20 h constant current test at 100 mA cm^{-2}.

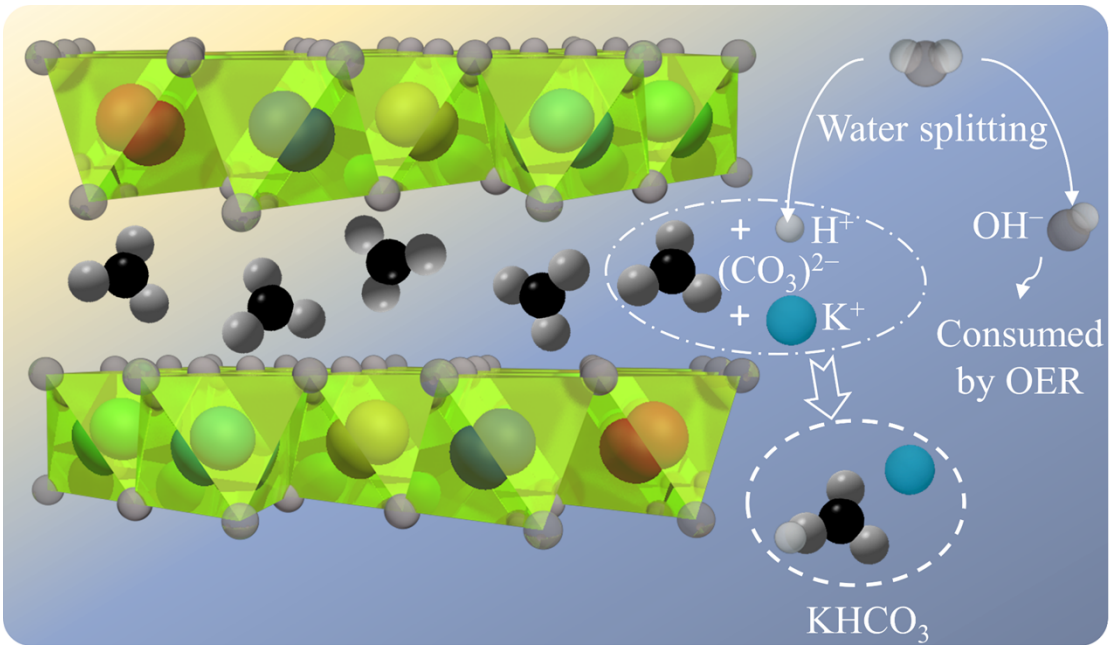

Figure S22 The schematic diagram for the formation $KHCO_3$.

Table S1 Proportion of different elements at corresponding STEM area.

Element	Weight %	Atomic %	Correction
C(K)	49.94	72.33	0.28
O(K)	14.98	16.28	0.51
Al(K)	3.31	2.14	0.92
Fe(K)	9.72	3.03	0.99
Co(K)	3.83	1.13	0.99
Ni(K)	4.46	1.33	0.99
Cu(K)	13.76	3.76	0.99
Total	100.00	100.00	

Table S2 Proportion of different elements corresponding to the elements mapping area by SEM.

Element	Wt. %	At. %
C(K)	48.53	64.78
O(K)	27.74	27.80
Al(K)	3.11	1.85
Co(K)	7.84	2.13
Ni(K)	7.86	2.15
Fe(K)	1.14	0.33
Cu(L)	3.72	0.94
Si(K)	0.06	0.02
Total	100.00	100.00

Table S3 ICP-OES results of different metallic elements in M^5

Elements	Molar ratio (at. %)	Approximate configuration entropy
Al	23.7	1.6 R
Fe	18.9	
Co	17.8	
Ni	18.9	
Cu	20.7	

Table S4 Comparing the OER overpotentials and specific capacitance of this work with diverse LDH and High entropy materials.

Material	OER overpotential (mV, at 10 mA cm^{-2})	Specific capacitance (F g^{-1} at 1 A g^{-1})	Electrolyte	Reference
NiCo-LDH	388		1M KOH	[10]
NiFe-LDH	348		0.1 M KOH	[11]
NiFe-LDH	360		1M KOH	[12]
NiFe-LDH	345		1M KOH	[10]
CoFe-LDH	404		0.1 M KOH	[11]
$Co_{1.8}Ni$-LDH	290		1 M KOH	[13]
CoFe-LDH@NiFe-LDH	360		1 M KOH	[14]
CoAl-LDH	340		1 M KOH	[15]
$La_{0.6}Sr_{0.4}Co_{0.8}Fe_{0.2}O_3$	353		1 M KOH	[16]
$La_{0.6}Sr_{0.4}Co_{0.8}Fe_{0.1}Mn_{0.1}O_{3-\delta}$	343		1 M KOH	[17]
$LiFe_{0.8}Co_{0.1}Ni_{0.1}O_2$	400		0.1 M KOH	[18]
Fe-Cr-Co-Ni-Cu-LDH	330		1 M KOH	[19]
Fe-Cr-Co-Ni-Cu-LDH	430		1 M KOH	[19]
NiCo-LDH		1962	6 M KOH	[20]
NiCo-LDH/NF		2103	2 M KOH	[21]
MnOOH/NiAl-LDH		1331.11	6 M KOH	[22]
MgCoAl-LDH		381.3	1 M KOH	[23]
$(FeCoCrMnZn)_3O_4$		340.3	1 M KOH	[24]
$(CoCrFeMnNi)_3O_4$		228	2 M KOH	[25]
FeOOH/NiCoAlFeCu-LDH	288	215.4	1 M KOH	This work

References

1. N. F. Mott, E. A. Davis and K. Weiser, Electronic processes in non-crystalline materials, *Physics Today*, 1972, **25**, 55.
2. P. Makula, M. Pacia and W. Macyk, How to correctly determine the band gap energy of modified semiconductor photocatalysts based on UV-Vis spectra, *Journal of Physical Chemistry Letters*, 2018, **9**, 6814-6817.
3. Z. Yang, X. Xie, J. Wei, Z. Zhang, C. Yu, S. Dong, B. Chen, Y. Wang, M. Xiang and H. Qin, Interface engineering $Ni/Ni_{12}P_5@CN_x$ Mott-Schottky heterojunction tailoring electrocatalytic pathways for zinc-air battery, *Journal of Colloid Interface Science*, 2023, **642**, 439-446.
4. Y. Xiao, C. Feng, J. Fu, F. Wang, C. Li, V. F. Kunzelmann, C.-M. Jiang, M. Nakabayashi, N. Shibata, I. D. Sharp, K. Domen and Y. Li, Band structure engineering and defect control of Ta_3N_5 for efficient photoelectrochemical water oxidation, *Nature Catalysis*, 2020, **3**, 932-940.
5. M. K. Adak, A. Rajput, D. Ghosh and B. Chakraborty, Role of Fe–O–M bond in controlling the eectroactive species generation from the $FeMO_4$ (M: Mo and W) electro(pre)catalyst during OER, *ACS Applied Energy Materials*, 2022, **5**, 13645-13660.
6. H. Jin, X. Liu, P. An, C. Tang, H. Yu, Q. Zhang, H. J. Peng, L. Gu, Y. Zheng, T. Song, K. Davey, U. Paik, J. Dong and S. Z. Qiao, Dynamic rhenium dopant boosts ruthenium oxide for durable oxygen evolution, *Nature Communications*, 2023, **14**, 354.
7. Zeenat, Z. Ahmad, A. Maqbool, M. Asif Hussain, R. Adel Pashameah, A. Shahzadi, N. Nazar, S. Iqbal, A. K. Alanazi, M. Naeem Ashiq and H. M. Abo-Dief, One-pot solvothermal synthesis of highly catalytic Janus transition metal phosphides (TMPs) for high performance OER, *Fuel*, 2023, **331**, 125913-125921.
8. W. Zhang, Z. Shahnavaz, X. Yan, X. Huang, S. Wu, H. Chen, J. Pan, T. Li and J. Wang, One-step solvothermal synthesis of raspberry-like NiCo-MOF for high-performance flexible supercapacitors for a wide operation temperature range, *Inorganic Chemistry*, 2022, **61**, 15287-15301.
9. F. Bahmani, S. H. Kazemi, H. Kazemi, M. A. Kiani and S. Yoones Feizabadi, Nanocomposite of copper–molybdenum–oxide nanosheets with graphene as high-performance materials for supercapacitors, *Journal of Alloys and Compounds*, 2019, **784**, 500-512.
10. F. Song and X. Hu, Exfoliation of layered double hydroxides for enhanced oxygen evolution catalysis, *Nature Communications*, 2014, **5**, 4477.
11. F. Dionigi, Z. Zeng, I. Sinev, T. Merzdorf, S. Deshpande, M. B. Lopez, S. Kunze, I. Zegkinoglou, H. Sarodnik, D. Fan, A. Bergmann, J. Drnec, J. F. Araujo, M. Gliech, D. Teschner, J. Zhu, W. X. Li, J. Greeley, B. R. Cuenya and P. Strasser, In-situ structure and catalytic mechanism of NiFe and CoFe layered double hydroxides during oxygen evolution, *Nature Communications*, 2020, **11**, 2522.

12. S. Jaskaniec, C. Hobbs, A. Seral-Ascaso, J. Coelho, M. P. Browne, D. Tyndall, T. Sasaki and V. Nicolosi, Low-temperature synthesis and investigation into the formation mechanism of high quality Ni-Fe layered double hydroxides hexagonal platelets, *Science Report*, 2018, **8**, 4179.
13. W. Hu, Q. Liu, T. Lv, F. Zhou and Y. Zhong, Impact of interfacial CoOOH on OER catalytic activities and electrochemical behaviors of bimetallic Co_xNi-LDH nanosheet catalysts, *Electrochimica Acta*, 2021, **381**, 138276.
14. R. Yang, Y. Zhou, Y. Xing, D. Li, D. Jiang, M. Chen, W. Shi and S. Yuan, Synergistic coupling of CoFe-LDH arrays with NiFe-LDH nanosheet for highly efficient overall water splitting in alkaline media, *Applied Catalysis B: Environmental*, 2019, **253**, 131-139.
15. Y. Song, Z. Li, K. Fan, Z. Ren, W. Xie, Y. Yang, M. Shao and M. Wei, Ultrathin layered double hydroxides nanosheets array towards efficient electrooxidation of 5-hydroxymethylfurfural coupled with hydrogen generation, *Applied Catalysis B: Environmental*, 2021, **299**, 120669.
16. L. Zhang, H. Zhu, J. Hao, C. Wang, Y. Wen, H. Li, S. Lu, F. Duan and M. Du, Integrating the cationic engineering and hollow structure engineering into perovskites oxides for efficient and stable electrocatalytic oxygen evolution, *Electrochimica Acta*, 2019, **327**, 135033.
17. L. Tang, T. Fan, Z. Chen, J. Tian, H. Guo, M. Peng, F. Zuo, X. Fu, M. Li, Y. Bu, Y. Luo, J. Li and Y. Sun, Binary-dopant promoted lattice oxygen participation in OER on cobaltate electrocatalyst, *Chemical Engineering Journal*, 2021, **417**, 129324.
18. L. Gui, G. Pan, X. Ma, M. You, B. He, Z. Yang, J. Sun, W. Zhou, J. Xu and L. Zhao, In-situ exsolution of CoNi alloy nanoparticles on $LiFe_{0.8}Co_{0.1}Ni_{0.1}O_2$ parent: New opportunity for boosting oxygen evolution and reduction reaction, *Applied Surface Science*, 2021, **543**, 148817.
19. K. Gu, X. Zhu, D. Wang, N. Zhang, G. Huang, W. Li, P. Long, J. Tian, Y. Zou, Y. Wang, R. Chen and S. Wang, Ultrathin defective high-entropy layered double hydroxides for electrochemical water oxidation, *Journal of Energy Chemistry*, 2021, **60**, 121-126.
20. X. Zhang, W. Lu, Y. Tian, S. Yang, Q. Zhang, D. Lei and Y. Zhao, Nanosheet-assembled NiCo-LDH hollow spheres as high-performance electrodes for supercapacitors, *Journal of Colloid and Interface Science*, 2022, **606**, 1120-1127.
21. A. Tang, P. Chen and C. Mi, Ni-Co layered double hydroxide nanosheet array on nickel foam coated graphene for high-performance asymmetric supercapacitors, *Ionics*, 2020, **26**, 6277-6287.
22. X. Hua, C.-J. Mao, J.-S. Chen, P.-P. Chen and C.-F. Zhang, Facile synthesis of new-type MnOOH/NiAl-layered double hydroxide nanocomposite for high-performance supercapacitor, *Journal of Alloys and Compounds*, 2019, **777**, 749-758.
23. Y. Zhang and S. Wei, Mg-Co-Al-LDH nanoparticles with attractive electrochemical performance for supercapacitor, *Journal of Nanoparticle*

Research, 2019, **21**, 14.
24. B. Liang, Y. Ai, Y. Wang, C. Liu, S. Ouyang and M. Liu, Spinel-type $(FeCoCrMnZn)_3O_4$ high-entropy oxide: Facile preparation and supercapacitor performance, *Materials*, 2020, **13**, 5798.
25. B. Talluri, M. L. Aparna, N. Sreenivasulu, S. S. Bhattacharya and T. Thomas, High entropy spinel metal oxide $(CoCrFeMnNi)_3O_4$ nanoparticles as a high-performance supercapacitor electrode material, *Journal of Energy Storage*, 2021, **42**, 103004.